ACS NANO

www.acsnano.org

ARTICLE

An Elastic and Damage-Tolerant Dry Epidermal Patch with Robust Skin Adhesion for Bioelectronic Interfacing

Yin Cheng,[#] Yi Zhou,[#] Ranran Wang,[#] Kwok Hoe Chan, Yan Liu, Tianpeng Ding, Xiao-Qiao Wang, Tongtao Li, and Ghim Wei Ho*

Cite This: *ACS Nano* 2022, 16, 18608–18620

Read Online

ACCESS | Metrics & More | Article Recommendations | Supporting Information

ABSTRACT: On-skin patches that record biopotential and biomechanical signals are essential for wearable healthcare monitoring, clinical treatment, and human–machine interaction. To acquire wearing comfort and high-quality signals, patches with tissue-like softness, elastic recovery, damage tolerance, and robust bioelectronic interface are highly desired yet challenging to achieve. Here, we report a dry epidermal patch made from a supramolecular polymer (SESA) and an in situ transferred carbon nanotubes' percolation network. The polymer possesses a hybrid structure of copolymerized permanent scaffold permeated by multiple dynamic interactions, which imparts a desired mechanical response transition from elastic recoil to energy dissipation with increased elongation. Such SESA-based patches are soft (Young's modulus ~0.1 MPa) and elastic within physiologically relevant strain levels (97% elastic recovery at 50% tensile strain), intrinsically mechanical-electrical damage-resilient (~90% restoration from damage after 5 min), and interference-immune in dynamic signal acquisition (stretch, underwater, sweat). We demonstrate its versatile physiological sensing applications, including electrocardiogram recording under various disturbances, machine-learning-enabled hand-gesture recognition through electromyogram measurement, subtle radial artery pulse, and drastic knee kinematics sensing. This epidermal patch offers a promising noninvasive, long-duration, and ambulant bioelectronic interfacing with anti-interference robustness.

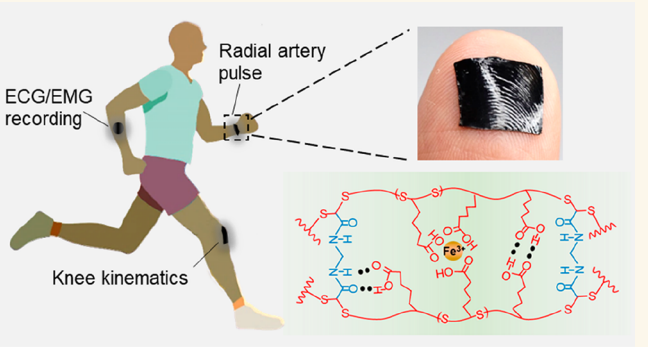

KEYWORDS: *epidermal patches, soft electronics, damage-tolerant, robust adhesion, interference-immune, bioelectronic sensing*

INTRODUCTION

Epidermal patches represent an intriguing wearable technology to capture and transmit various kinds of body information, considering their suitable formfactor for direct on-skin deployment and easy integration with other electronic components into sophisticated layered functional systems.[1−5] Specifically, intensive research efforts focus on acquiring electrophysiological and biomechanical signals, as they play a vital role in diverse applications, ranging from a human–machine interface, wearable healthcare and athletic rehabilitation,[6,7] to early stage diagnosis and clinical treatment.[8]

In daily use, it is desired that epidermal patches exhibit tissue-like softness and good elasticity:[9,10] patches with Young's modulus on par with or lower than that of human skin (0.1−2 MPa)[11,12] can improve wearing comfort by relieving mechanical constraints on skin; and excellent elasticity allows patches to freely accommodate skin deformation, without compromising sensing performance in capacitive or piezo-resistive mechano-electrical transducers caused by pronounced plastic deformation. As the epidermal patches are mostly soft and susceptible to structural failures, such as cut and laceration, the ability to tolerate and even self-repair mechanical damages can significantly enhance the functional robustness and extend the device lifetime. Besides, a conformable and adhesive patch–skin interface is crucial for signal fidelity: The conformable match on wrinkled skin topology increases the effective contact area, and the strong

Received: July 17, 2022
Accepted: October 28, 2022
Published: November 1, 2022

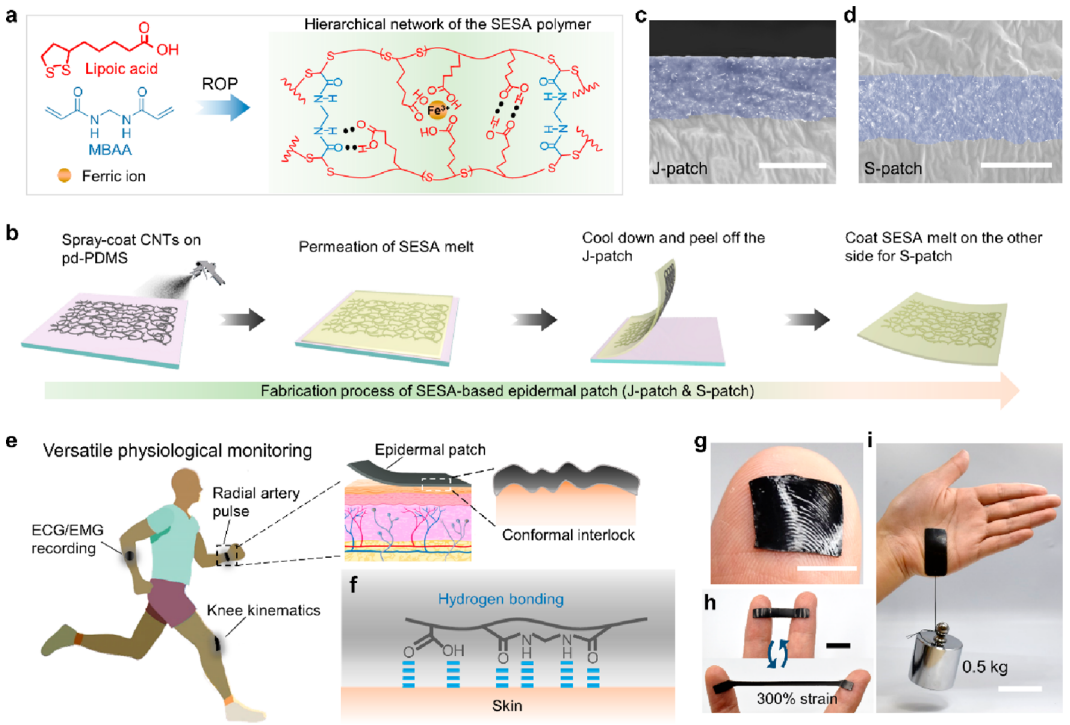

Figure 1. The SESA polymer synthesis and the fabrication of SESA-based epidermal patches. (a) Synthetic route and hierarchical network of SESA polymer. (b) The fabrication process of SESA-based epidermal patches, including J-patch and S-patch. (c-d) Cross-sectional SEM image of J-patch (c) and S-patch (d). The colorized (purple) areas indicate the CNT-SESA composite layer. Scale bars, 10 μm. (e) Schematic illustration of versatile physiological monitoring using epidermal patches, including J-patch for ECG/EMG recording and S-patch for pulse and motion sensing. (f) Schematic of the interfacial interactions between the SESA network and skin. (g) A piece of J-patch attached on thumb with the surface relief structures transferred from the underlying fingerprint. Scale bar, 10 mm. (h) A strip of J-patch adhered onto two fingers and stretched to show elastic resilience at 300% tensile strain. Scale bar, 15 mm. (i) A piece of J-patch bearing a weight of 0.5 kg attached tightly onto palm. A stiff PET backing on the outer surface of J-patch ensured the weight was completely supported by the interfacial adhesion force. The size of patch is 20 × 45 mm^2. Scale bar, 45 mm.

adhesion anchors the intimate bonding at the interface, both of which facilitate reliable electrophysiological and biomechanical sensing. In general, considering wearing comfort and robust signal acquisition, epidermal patches are required to be tissue-like soft and elastic, damage-tolerant, and adherent to skin conformably.

Rubbery elastomers, such as polydimethylsiloxane (PDMS), polyurethane (PU), and poly(styrene-ethylene-butylene-styrene) (SEBS) copolymer, are frequently utilized for construction of epidermal sensors. Someya's group[13] has reported the exploitation of polyurethane-polydimethylsiloxane (PU-PDMS) nanomeshes with superb softness and elasticity as on-skin strain gauges, which exhibited minimum mechanical interference in body movement detection and high signal reproducibility in cyclic strain sensing. However, epidermal patches based on purely covalently cross-linked elastomers with no dynamic motifs lack the capacity to tolerate or self-repair structural damages. Self-healing polymers based on dynamic physical interactions are promising choices for damage-resilient soft electronics and have been employed in biomechanical[14−18] and biopotential[19,20] sensing. Nevertheless, such viscoelastic self-healing polymers often show obvious plastic deformation due to the reconstruction of physical cross-links at large strains,[21−25] which can lead to inaccurate biomechanical sensing during cyclic testing. To obtain a reliable sensing interface, a pregelled Ag/AgCl electrolytic electrode is widely employed in clinical settings for biopotential recording, as it provides high-quality signals due to its conductive and adhesive nature. However, long duration wearing of the wet gel can cause skin discomfort and irritation, as well as signal degradation induced by gel dehydration. Another strategy to realize good adhesion with skin is to design electronic patches with ultrathin geometries (typically with a thickness under 10 μm).[26−31] The ultrathin thickness contributes to easy attachment and anchoring through just van der Waals interaction. Nonetheless, such structures are not sufficiently self-supporting, suggesting problematic handling and processing during fabrication, transfer, and recycling.

Recently, adhesive and dry polymer patches have been attracting increasing interest to serve as electrophysiological and biomechanical sensors, as they afford strong bonding to skin and avoid the issues of dehydration at elevated temperature and solvent leakage under deformation that are characteristic for hydrogels. Although considerable progress has been made, there exist performance concerns that hinder their real-world applications, including poor elastic recovery at physiologically relevant strain level (~40% tensile strain),[32,33] susceptibility to structural damages, and unproved capability to retain high quality signal in various disturbance conditions (body motion, sweat, underwater, etc.).[34−40] Until now, it is still a formidable challenge to develop dry patches as bioelectronic electrodes that are soft and elastic, damage-tolerant, and interface-reliable against multiple interferences.

Herein, we introduce a material strategy for the design of a dry epidermal patch for bioelectronic interfacing. The construction relies on the in situ transfer of carbon nanotube

https://doi.org/10.1021/acsnano.2c07097
ACS Nano 2022, 16, 18608−18620

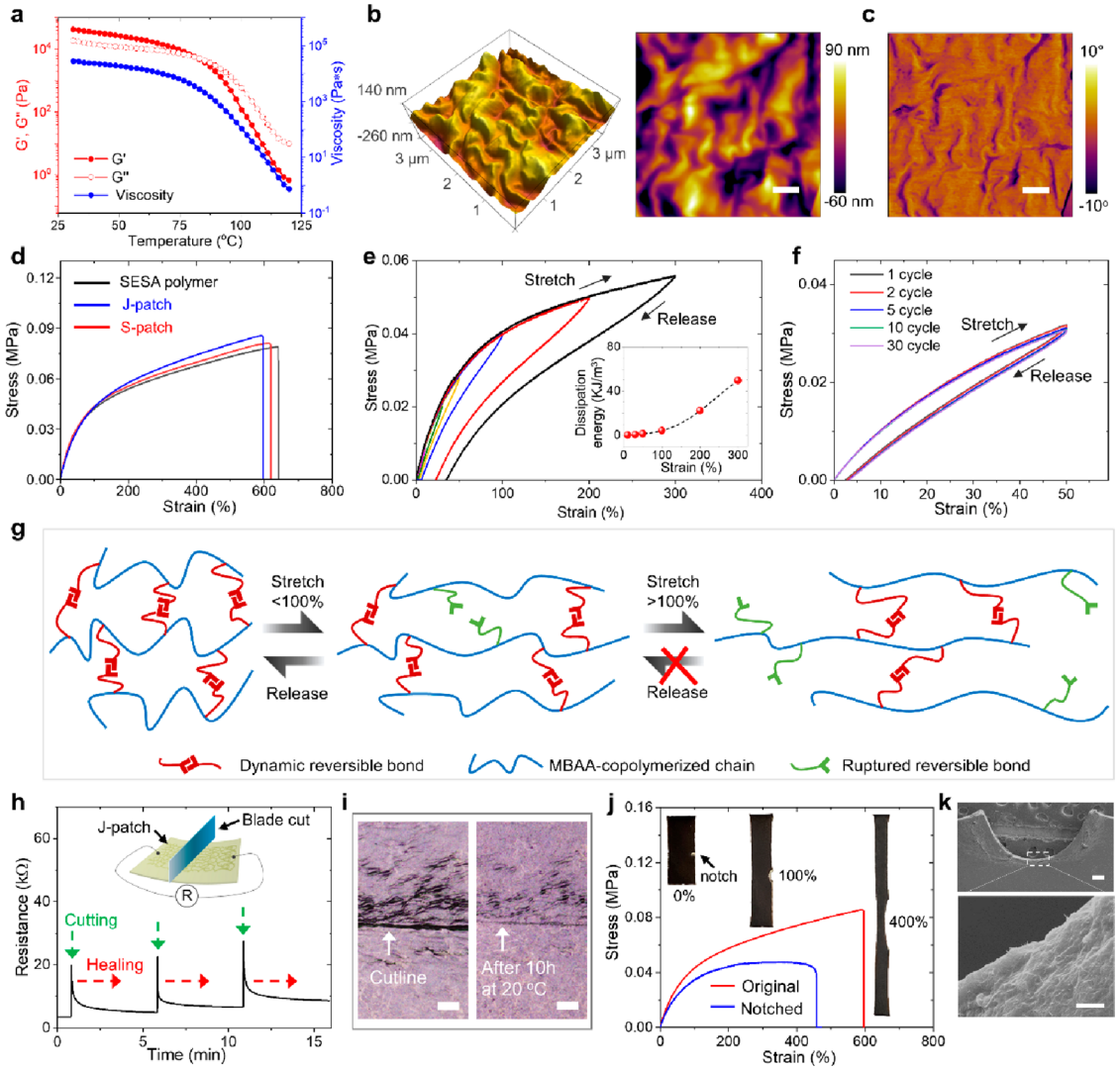

Figure 2. Thermal, mechanical, self-healing, and notch-insensitive characterization of the SESA-based epidermal patch. (a) Temperature-dependent rheological characterization of SESA polymer. (b) 2D (right) and 3D (left) topographical AFM images of the J-patch. Scale bar, 500 nm. (c) Phase AFM image of the J-patch. Scale bar, 500 nm. (d) Tensile stress–strain curves of SESA polymer, J-patch, and S-patch. (e) Tensile loading–unloading curves at different strains (10%, 30%, 50%, 100%, 200%, 300%) of J-patch. The inset shows the dissipation energy at each loading–unloading cycle. (f) Tensile stretch-release cycles of J-patch. Rest time of 15 s in between each loading cycle to allow delayed recovery. (g) The sequential mechanical response of SESA polymer under increased tensile strain: elastic recoil within 100% strain and energy dissipation over 100% strain. (h) Electrical resistance of J-patch as a function of time while undergoing 3 cuttings using a razor blade at 0.5N normal force at different positions. (i) Optical microscopic images of self-healable J-patch before and after self-healing at 20 °C for 10 h. Scale bars, 10 μm. (j) Tensile stress–strain curves of original and notched (1 mm notch for a sample of 5 mm in width and 12 mm in length) J-patches. Insets show notched J-patch at 0%, 100% and 400% strain. (k) SEM images of the notch at 100% strain. Scale bars are 200 μm (top) and 2 μm (bottom).

percolation network onto solvent-free supramolecular, elastic, self-healing, and adhesive (SESA) polymer surface to obtain Janus and Sandwiched patches (J-patch and S-patch), targeting biopotential and biomechanical signals, respectively. The supramolecular polymer SESA stemmed from a copolymerized covalent network, permeated by multiple dynamic interactions. Such hybrid polymer exhibits mechanical response from elastic recoil to energy dissipation along with increased elongation. It enables the epidermal patch to unify the challenging needs in a single platform, including skin-like softness (Young's modulus ~0.1 MPa), excellent resilience (92.7% elastic recovery at 100% tensile strain), electrical self-healing (91.4% restoration after 5 min), notch-insensitive stretchability (as high as 460%), and robust on-skin adhesion under various harsh conditions (stretch/underwater/sweat). These combinational attributes make it well-suited for on-skin high-fidelity signal capturing, especially in long-duration, ambulatory use. We demonstrated versatile physiological signal acquisition, from electrocardiogram (ECG) recording under different disturbances, machine-learning-enabled hand gesture identification through electromyogram (EMG) measurement, to radial artery pulse and knee motion sensing. The various scenarios validate the great potential in future outdoor healthcare applications.

RESULTS AND DISCUSSION

Design of SESA-Based Epidermal Patches. To unite the seemingly antagonistic merits of being highly elastic yet readily self-healable and self-adhesive,[41] we chose a biological

https://doi.org/10.1021/acsnano.2c07097
ACS Nano 2022, 16, 18608–18620

molecule, ALA, as the starting material, for its tailored structure allowed the formation of covalent network with high density dynamic motifs. Figure 1a illustrates the simplified synthetic route and structure of SESA polymer (see detailed process in Methods, Figure S1 of SESA polymer photographs): (i) ALA went through ring opening polymerization at elevated temperature (140 °C) through thermal-initiated cleavage of disulfide bonds; (ii) *N*,*N*′-Methylenebis(acrylamide) (MBAA) was introduced into liquid ALA for copolymerization to afford chemically stable covalent copolymer; (iii) Ferric ion (Fe^{3+}) was further added into the ALA-MBAA copolymer melt to work as strong complex centers with carboxylic groups from ALA and then cooled down to room temperature to get the SESA polymer. Multiple spectroscopic analyses were implemented to testify the polymer structure. X-ray diffraction (XRD) showed no crystalline peaks, suggesting the amorphous state and no formation of iron oxide in the matrix. Time of flight secondary ion mass spectrometry (TOF-SIM) characterization further verified the existence of ferric ions dispersed in the polymer (XRD and TOF-SIM results in Figure S2). Raman spectra displayed a splitting of peak at 507 cm^{-1} (corresponding to disulfide bonds of ALA) into two marked peaks at 506 and 521 cm^{-1} for SESA, proving the occurrence of ring-opening polymerization (Figure S3). In the Fourier transform infrared (FTIR) test (Figure S4), the newly emerged peaks at 1538 (N−H bending) and 3290 cm^{-1} (N−H stretch secondary amine) in SESA agreed with the copolymerization of MBAA, and the red shifting of the carbonyl group stretching frequency (from 1686 to 1700 cm^{-1}) along with the emergence of a new peak at 1655 cm^{-1} substantiated the formation of Fe^{3+}-carboxyl coordinative bond.

The fabrication process of SESA-based epidermal patches is shown in Figure 1b (detailed process in Methods): We sprayed aqueous CNT dispersion on hydrophilic polydopamine modified PDMS (pd-PDMS) substrate (contact angle tests in Figure S5), and then the conductive CNT percolation network was in situ transferred and embedded into SESA film surface in Janus (J-patch) or sandwiched (S-patch) form. The sheet resistance of the prefabricated CNT film on pd-PDMS was tunable through spray-coating cycles, and it increased after the embedding process, likely due to the penetration of polymer melt between the CNTs (Figure S6). CNT film with a sheet resistance of 25 Ω/□ before transfer was adopted for use. The sheet resistance of the patch after transfer was about 134 Ω/□. To allow smooth manipulation for on-skin use (easy and intact attachment/detachment by hand), the thickness of J-patch and S-patch was tuned and increased to be around 140 μm (Figure S7). Cross-sectional view scanning electron microscope (SEM) images in Figure 1c (J-patch) and 1d (S-patch) clearly reveal the composite CNT-SESA embedding layer to be around 8 μm. Figure 1e schematically conceptualizes the versatile physiological monitoring using SESA-based patches as bioelectronic interfacing electrodes: J-patch for biopotential and S-patch for biomechanical sensing. The SESA-based patches readily form a conformal interlock with skin texture upon attachment (confirmed later), owing to the tissue-like softness and geometric thinness. Furthermore, the patches with abundant functional groups of −COOH, C═O and N−H on the surface can have strong physical adsorption to the outermost stratum corneum (mostly consisting of keratin, ceramide, cholesterol, and free fatty acid) through hydrogen bond formation (Figure 1f). The mechanical interlock and interfacial bonding cooperatively allow for robust skin adhesion in various conditions. In Figure 1g, when a piece of J-patch was pressed onto the thumb, the surface relief of the underlying thumbprint was transferred to the J-patch, suggesting the ultraconformal matching at the interface. Figure 1h demonstrates the J-patch was able to sustain a stretch of 300% strain with elastic resilience. The secure bond to the skin was demonstrated by hanging a weight of 0.5 kg to a J-patch attached to the palm without interfacial failure.

Thermal, Mechanical, Self-Healing, and Notch-Insensitive Properties of SESA-Based Epidermal Patches. Various tests were conducted to investigate the thermal behavior of SESA polymer. Thermogravimetric analysis (TGA, Figure S8) revealed that SESA polymer started to decompose at 200 °C, verifying high thermal stability. The glass transition temperature (Tg) was determined to be −37.7 °C from the differential scanning calorimetry (DSC, Figure S9). Such low Tg suggested elastic behavior at a wide temperature range, and favorable high chain mobility at room temperature for self-healing. In temperature sweeping rheological test (Figure 2a), storage modulus (G') and loss modulus (G'') both decreased as the temperature increased, and G' was higher than G'' until 85 °C, indicating solid-like to liquid-like transition of mechanical response. Moreover, the apparent viscosity of SESA polymer went through a continuous decrease along with a rise in temperature, probably due to the heat-labile hydrogen bonds, disulfide bonds, and enhanced chain mobility. This temperature-dependent rheology enables the easy thermo-processing of SESA polymer for molding and recycling.

The surface morphology of the J-patch at the SESA-CNT side was characterized by atomic force microscopy (AFM). Both 2D and 3D topological AFM images in Figure 2b show the surface roughness is about 34 nm. The smooth patch surface is beneficial to close and conformal match with a rugged skin contour. The phase AFM image in Figure 2c reveals a homogeneous phase of the SESA-CNT layer, implying the embedding of CNT network does not affect the copolymerization of SESA polymer. In mechanical characterization, Figure 2d displays the tensile stress−strain curves of SESA polymer, J-patch, and S-patch, which indicated a similar behavior of high stretchability of about 600% strain and skin-like Young's modulus of 0.1 MPa (calculated from linear part within 5% strain). The tensile loading−unloading curves of J-patch at varying strains from 10% to 300% is shown in Figure 2e, and the corresponding dissipation energy (hysteresis area) was measured in the inset. Clearly, under the strain of 100%, the immediate residual strain was minimal (3.8% for 50% and 7.3% for 100% test strain). Also, note that the residual strain after 50% test strain could be almost completely recovered with a prolonged resting time of around 15 s. The inset shows the dissipation energy rose sharply when the stretch strain surpassed 100%. The outstanding elastic resilience within physiological strain level (∼40%) was further confirmed by performing cyclic tensile stretch-release tests at a strain of 50% in Figure 2f, as the mechanical response curves did not show noticeable degradation in strength and aggravation in residual strain. Based on these results, we proposed a likely mechanism to interpret the mechanical response of SESA-based patches (Figure 2g). Within a modest strain level (<100%), the patch mainly experiences an elastic deformation, which is dominated by the stretch and conformational-entropy-driven retraction of a permalent scaffold (ALA copolymerized with MBAA), with negligible amounts of dynamic bonds being ruptured. Under

https://doi.org/10.1021/acsnano.2c07097
ACS Nano 2022, 16, 18608−18620

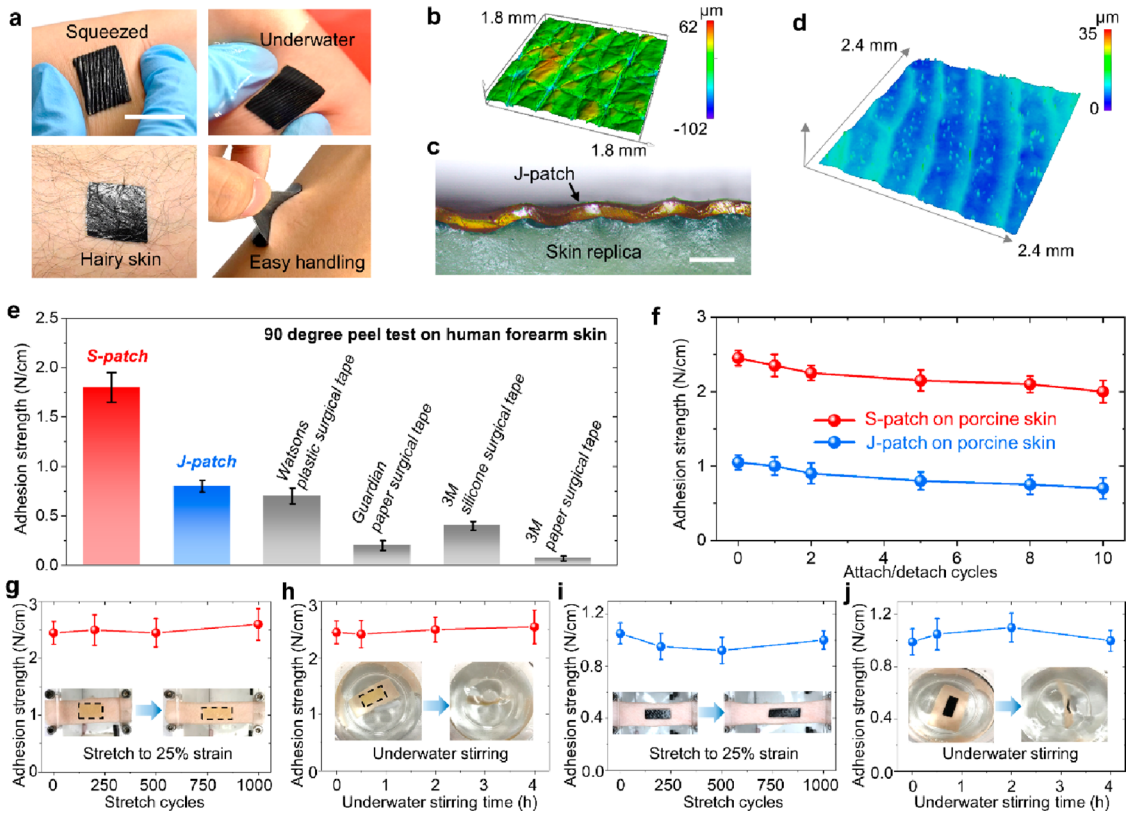

Figure 3. The on-skin conformability and robust adhesiveness of SESA-based epidermal patch. (a) Photographs of J-patches (22 × 22 mm^2) on forearm skin in different conditions: squeezed, underwater, hairy skin, and handled by hand. Scale bar, 20 mm. (b) 3D laser-scanning microscopic image of a PDMS skin replica surface. (c) Optical microscopic image shows the conformal attachment of J-patch on the PDMS skin replica. Scale bar, 500 μm. (d) The 3D laser-scanning microscopic image of a J-patch surface (the contact side) after being pressed onto fingertip for 5s and then detached. (e) Adhesion strength comparison of SESA-based epidermal patches (S-patch and J-patch) and commercial medical tapes (four kinds of tapes from brands of Watsons, Guardian, and 3M). 90 deg peel tests were conducted on human forearm skin. (f) Adhesion strength of S-patch and J-patch on porcine skin for 10 cyclic attach/detach events. (g,i) Adhesion strength change of S-patch (g) and J-patch (i) on porcine skin during 1000 stretch cycles at strain of 25%. (h,j) Adhesion strength change of S-patch (h) and J-patch (j) on porcine skin during underwater stirring (300r/min) for 4 h.

larger strains (>100%), the network continued to stretch to result in sliding of MBAA copolymerized chains. This slippage led to considerable dissociation of reversible bonds and reassociation at new sites, which contributed to the enhancement of toughness and damage tolerance through efficient energy dissipation.[21,22] Such scheme of sequential mechanical response provides both a decent elastic recoil within physiologically related strain level and high damage tolerance (discussed later) for the SESA-based patches.

The copious dynamic bonds (disulfide bond, hydrogen bond and metal−ligand coordinative bond) within SESA endow it with superb mechanical self-healing capability even at room temperature (Figure S10): Healing efficiency of 62% and 87%, in terms of maximum tensile strain, were achieved after healing durations of 2 and 5 min respectively, when a SESA sample was severed and reconnected again. Such efficient structural restoration upon damage facilitates the self-reconstruction of conducting network of SESA-CNT composite layer, resulting in the recovery of electrical property.[3] Figure 2h shows the electrical resistance evolution of a J-patch sample when we inflicted a surface-level cut on the conductive SESA-CNT side using a razor blade at 0.5N normal force for 3 times (time intervals of 5 min). Interestingly, the electrical conductivity went through autonomous recovery rapidly, without the need to push the cut interfaces into contact. For the first cutting, the resistance increased immediately from 3.5 KΩ to 19.8 KΩ, and then dropped to 4.9 KΩ after 5 min self-healing at 20 °C, indicating a restoration efficiency of 91.4% in terms of the recovered resistance increment. The electrical self-healing could be attributed to the initial physical contact of the cut interfaces and then the rearrangement of the conductive nanonetwork driven by the dynamic nature of SESA (high chain mobility and dynamic bonds). The almost indiscernible cutline after healing for 10h at 20 °C in Figure 2i further evinced the reconnection of the SESA-CNT conductive network. Besides, the mechanical self-healing was also verified through the resistance variation versus stretch (Figure S11): the self-healed J-patch succeeded in withstanding a tensile loading−unloading event at 100% strain, in contrast to the abrupt mechanical and electrical failure of a PDMS-CNT electrode (fabrication process in Methods) at 14% strain due to the rapid crack propagation. We further performed the tensile stretching test to J-patch samples with and without a single-edge notch (1 mm notch for a sample with a width of 5 mm). Figure 2j shows the notched sample still retained a stretchability as high as 460%. Figure 2k displays the pronounced blunting of the crack at 100% strain of the notched sample. These observations evidence that SESA-based patch is able to spread concentrated stress at the crack tip via dissociation-reassociation of dynamic bonds and rearrange-

https://doi.org/10.1021/acsnano.2c07097
ACS Nano 2022, 16, 18608−18620

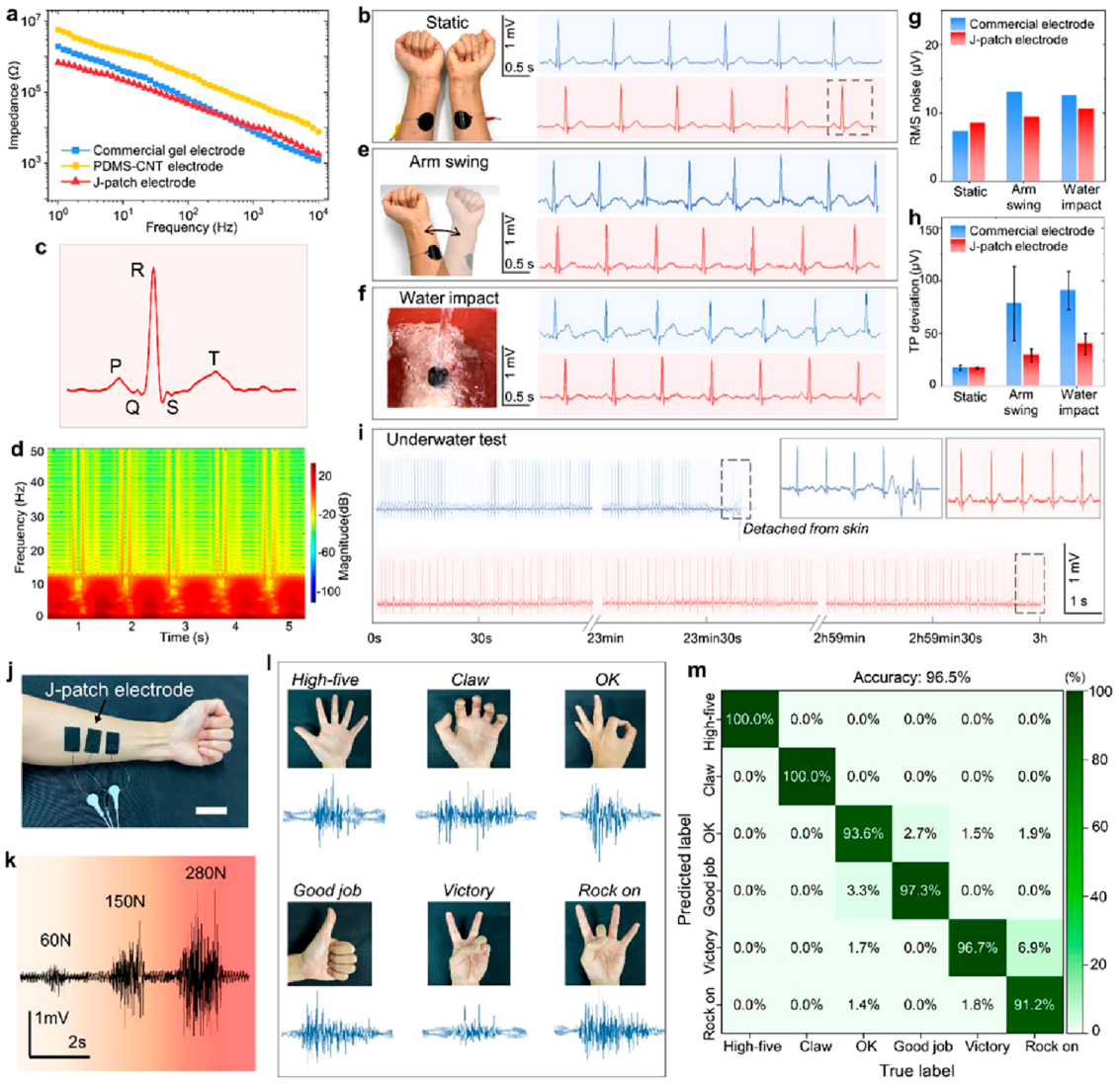

Figure 4. Biopotential signal detection using J-patch as electrophysiological electrodes. (a) The on-skin impedance analysis of commercial gel electrode (Ag/AgCl electrode), PDMS-CNT electrode, and J-patch electrode. PDMS-CNT electrodes were attached on forearm skin and fixed using medical tape. (b) Left: schematic shows the electrodes deployment in ECG test: RA (right arm), LA (left arm), LL (left leg); right: enlarged curve of one cardiac cycle by J-patch at static state. 3-Lead deployment method was adopted here for ECG measurement. (c) ECG measured by commercial and J-patch electrodes at static state. (d) Spectrogram analysis of five successive ECG pulses recorded using J-patch electrode. (e) ECG measured by commercial and J-patch electrodes during arm swing. (f) ECG measured by commercial and J-patch electrodes under water impact. (g) The calculated RMS noise of commercial and J-patch electrodes under different conditions. (h) The calculated TP deviation of commercial and J-patch electrodes under different conditions. (i) ECG measured by commercial and J-patch electrodes underwater for extended time. (j) Photograph shows J-patch electrodes (20 × 30 mm^2) on forearm with gap distance of 15 mm. Scale bar, 40 mm. (k) EMG signal measured at different gripping force of 60N, 150N, and 280N. (l) EMG patterns corresponding to finger motions that give six hand gestures. (m) Confusion matrix for hand gesture identification of six gestures, showing a high accuracy of 96.5%.

ment of entangled polymer chains.[14,42] Such mechanical-electrical damage-tolerant merits promise reliable and resilient real-world applications of the SESA-based epidermal patches with extended lifespan.

Robust Adhesion of SESA-Based Epidermal Patches. To show the strong adhesion of SESA-based epidermal patch, we attached J-patches to human skin under various conditions in Figure 3a: When the skin was squeezed, the ridge-like features on the patch suggested intimate adaptation both in the air (top-left) and underwater (top-right); The patch could also adhere tightly on hairy skin (bottom-left); Notably, it could be detached intactly with ease after long-time use (10 h) and exhibited no skin irritation and redness (Figure S12). The microscopic conformal interlock was probed by attaching a J-patch to a PDMS skin replica. The 3D laser-scanning confocal microscopic image of skin replica in Figure 3b revealed microgroove morphology with a vertical roughness of 115 μm (Figure S13). A seamless match at the interface was shown in the optical microscopic image (Figure 3c). We speculate it is the intrinsic softness of the SESA polymer that gives rise to the interlock at the interface. When attached and pressed onto the skin, the patch can deform easily and conform its localized surface curvature to the skin textures. This assumption is consistent with the observation that the fingerprint was transferred to the J-patch surface after being detached (Figure 3d).

To quantify the adhesive properties, we conducted 90-degree peel tests on human forearm skin, using S-patch, J-

https://doi.org/10.1021/acsnano.2c07097
ACS Nano 2022, 16, 18608−18620

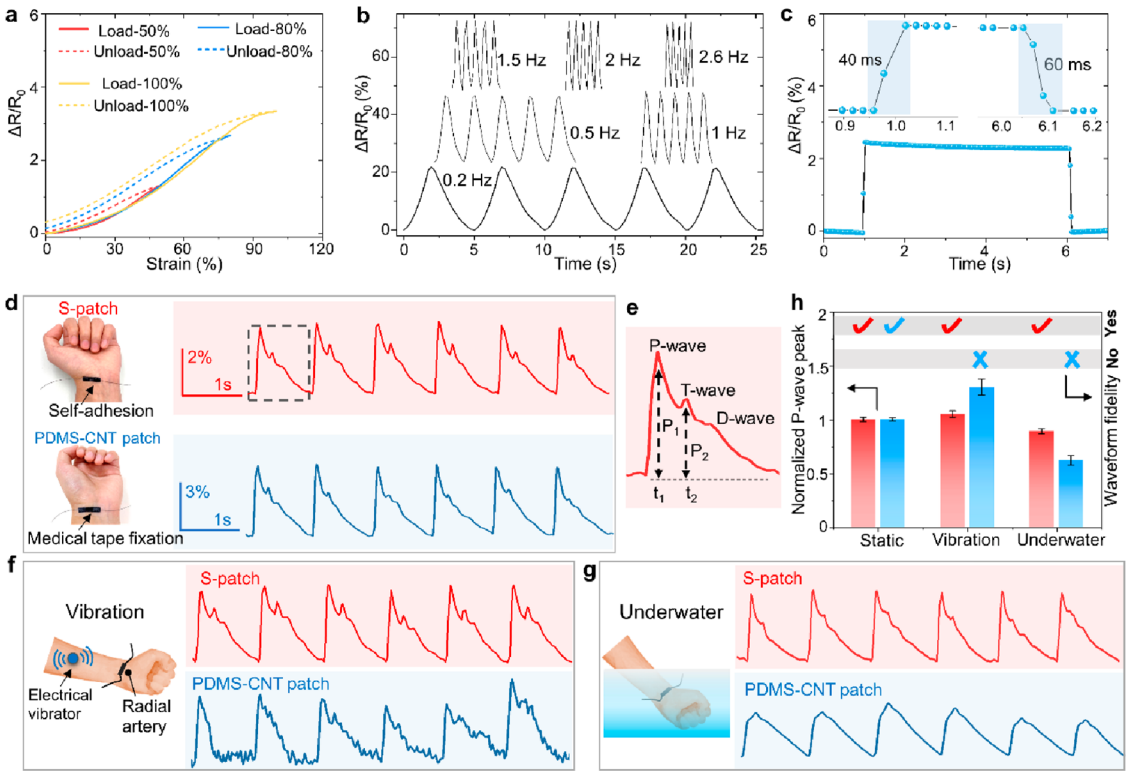

Figure 5. Strain sensing properties of S-patch sensor and radial artery pulse monitoring. (a) Relative resistance variation of S-patch sensor under loading−unloading cycle at strains of 50%, 80% and 100%. (b) Repeatable electrical responses under 20% strain at frequencies from 0.2 to 2.6 Hz. (c) Real time, fast response (~40 ms), and recovery (~60 ms) of the S-patch sensor upon application of a quasi-transient step strain of 5%. (d) The electrical response of six successive radial artery pulses recorded by S-patch and PDMS-CNT sensors. The S-sensor is self-adhesive and the PDMS-CNT sensor needs medical tape fixation. (e) The enlarged pulse signal of S-patch sensor from the dotted box in Figure 5d. (f) The electrical response of six successive radial artery pulses by S-patch and PDMS-CNT sensors when an electrical vibrator was attached on skin nearby. (g) The electrical response of six successive radial artery pulses by S-patch and PDMS-CNT sensors during underwater sensing. (h) The extracted normalized P-wave peak and waveform fidelity of S-patch (red) and PDMS-CNT (blue) sensors.

patch, and several commercial medical tapes (including plastic, paper, and silicone types) for comparison (Figure S14). From the results in Figure 3e, the S-patch exhibited the highest adhesion strength of 1.8 N/cm, and the J-patch had a lowered value of 0.8 N/cm. This decrease of adhesion force might be caused by the reduced areal presence of SESA polymer at the interface due to the partially occupied surface area by CNT. Despite this reduction, J-patch still displayed a higher adhesive strength than four tested commercial tapes and many reported adhesive epidermal electrodes.[23,39,43,44] We ascribe such strong on-skin adhesiveness to the synergistic effects of adaptive interlock and polymer-skin adsorptions. Also worth noting is that the strong adhesion occurs within 10 s at most (preparation time required for peel test), suggesting the potential application for instant adhesion.

We subsequently chose porcine skin for adhesion robustness evaluation in cyclic use and under extreme conditions, as it possesses mechanical robustness and close resemblance to human skin.[45] The SESA epidermal patches revealed similar adhesion strength on porcine skin as that on human skin (Figure S15). After 10 attach/detach cycles, the adhesion strength decreased from 2.45 to 2 N/cm for S-patch and 1.05 to 0.7 N/cm for J-patch respectively, both still high enough for secured bonding, proving the feasibility for repetitive use as dry electrodes. The adhesion strength decrease is likely brought about by the dirt contamination like sebum. We further assessed the adhesion strength of both S-patch and J-patch on porcine skin under cyclic stretching at 25% strain and underwater stirring. Even after 1000 stretch cycles or 4 h unremitting underwater stirring, the patches maintained a firm interface on porcine skin, with no obvious decline in adhesion strength (Figure 3g−j). This robust on-skin adhesion not only empowers high-quality biopotential and biomechanical signal harvesting but also promises the reliable monitoring of ambulant and continuous physiological activities, even under harsh environmental interferences.

Biopotential Recording. The interfacial impedance between human forearm skin and J-patch was analyzed for comparison with the results of commercial Ag/AgCl electrolytic gel electrode and PDMS-CNT electrode at a physiologically relevant frequency of $1-10^4$ Hz. As seen in Figure 4a, the PDMS-CNT electrode shows a saliently higher impedance because of the surface nonadhesiveness. In comparison with the nonadhesiveness of PDMS-CNT electrode with skin, the high adhesive strength of the J-patch assisted in the anchoring and fixation of the electrode surface to the skin, which favored the lowered interfacial impedance. The J-patch electrode reveals comparable impedance to that of commercial gel electrode and is slightly lower at the range of 1−100 Hz. At 100 Hz, the impedances for commercial gel electrode and J-patch are 63.6 and 41.8 KΩ, respectively.

We first used a J-patch for ECG recording to evaluate its efficacy as preparation-free dry biopotential electrodes, as ECG provides significant information to analyze heart rhythms and diagnose cardiovascular disease. To measure ECG signals, J-patch or commercial gel electrode pairs were attached to

https://doi.org/10.1021/acsnano.2c07097
ACS Nano 2022, 16, 18608−18620

human forearms (Figure 4b, left). The equivalent circuit diagram of the J-patch on skin is shown in Figure S16. In a static state, J-patch electrodes give rise to clear and stable signals, similar to those of Ag/AgCl electrodes (Figure 4c). An enlarged curve of one cardiac cycle by J-patch (black dotted box in Figure 4c) is shown in Figure 4b (right) to reveal a distinguishable rhythmics-relevant PQRST waveform. In addition, the spectrogram of ECG signal of J-patch in static state in Figure 4b was analyzed using Fast-Fourier Transform in Figure 4d: the clear frequency identification of heart rhythm is acquired, facilitating the clinical diagnosis of abnormalities of heart functions, such as the arrhythmia, myocardial ischemia, and potential heart failure.[46,47] ECG measurements under arm swing and water impact were further conducted and shown in panels e and f, respectively, of Figure 4. More severe signal distortion was observed for the commercial gel electrode. To quantify the motion artifact, root-mean-squared (RMS) noise (indicates signal fluctuation over time) and TP deviation (reflects baseline drift) were extracted from ECG signals of J-patch and commercial electrode, as seen in Figure 4g,h. In static status, the RMS noise of J-patch (8.5 μV) was slightly higher than that of the commercial electrode (7.3 μV). However, for the cases of arm swing and water impact, the RMS noise of J-patch remained more stable than the considerably increased values of commercial electrode. For TP deviation at static state, the J-patch and commercial electrode both revealed low deviation levels: 17.1 and 17.3 μV, respectively. Under arm swing and water impact, it increased to 29 and 40 μV for J-patch, and 78 and 90 μV for commercial electrode. These comparisons quantitatively prove that the J-patch electrode is superior to the commercial gel electrode for biopotential recording in terms of reducing motion artifact interferences. Lastly, long-duration underwater ECG testing was performed. The commercial gel electrode detached from the skin after 23 min, leading to measurement failure. In contrast, J-patch kept a tight skin-electrode interface and stable ECG signal for as long as 3 h. Therefore, the robust on-skin adhesion of the J-patch makes it highly suitable for ambulatory biopotential recording in wearable healthcare, especially when it involves motions and underwater submersion.

Next, the J-patch electrodes were attached to the forearm for EMG measurement that detect the action potential induced by hand muscles (electrodes deployment in Figure 4j). When the volunteer held a grip dynamometer using forces of 60, 150 and 280N, the generated EMG signals exhibited increasing peak-to-peak amplitude (Figure 4k), consistent with the gripping force variation. Furthermore, when the volunteer made different hand gestures, the acquired EMG revealed distinctive and repeatable patterns (Figure 4l, Figure S17), suggesting high-quality signals from J-patch. We took advantage of the EMG results for machine-learning-enabled smart hand gesture identification: three groups of EMG data for training and one for prediction (Figure S18, details in Methods). The corresponding confusion map for hand gesture recognition is shown in Figure 4m, which gives a high accuracy of 96.5%. This high recognition accuracy further validated that the J-patch electrode could establish a robust EMG capturing interface on skin to ensure highly reproducible signals. The machine-learning-enabled hand gesture identification through J-patch promises great potential in human-machine interaction when visual/vocal information is inaccessible.

Biomechanical Sensing and Radial Artery Pulse Recording. The S-patch is adopted as an on-skin strain sensor, considering its conformal attachment and the protected CNTs percolation network in the sandwiched structure. In Figure 5a, when stretched to strains of 50%, 80% and 100%, the relative increment of electrical resistance increased monotonously to 130%, 260%, and 330%, accompanied by hysteretic loops upon strain release, due to the piezo-resistive nature of CNT-polymer nanocomposite.[48,49] For a stretch strain of 50%, which covers human motion relevant strain level on the skin (~40%), the residual relative resistance increase was as small as 3.8%, favoring reproducible signal acquisition (Figure S19). The S-patch exhibited uniform and repeatable electrical response toward cyclic strain inputs at a broad frequency range from 0.2 to 2.6 Hz in Figure 5b, probably owing to the excellent elastic resilience of SESA polymer at modest strain levels. Fast response (~40 ms) and recovery (~60 ms) were verified in the quasi-transient step strain sensing (Figure 5c). The durability was assessed by implementing 4000 cycles of stretching/releasing at a strain of 50%, and the electrical response remained stable after a slight attenuation over the initial few hundreds of cycles, giving almost the same signal at cycle numbers of 2000 and 4000 (Figure S20).

We attached the S-patch sensor on the wrist to monitor radial artery pulse, as such subtle signal capturing requires not only high sensitivity but also tight bonding to skin for mechanical input fidelity, especially under environmental interferences. Figure 5d shows the S-patch (self-adhesive) and PDMS-CNT patch (using medical tape for fixation) on the wrist, and the recorded six successive pulse signals. The two sensors reported similar characteristic pulse waveforms, and succeeded in distinguishing the three clear peaks caused by the superposition of the incoming blood wave ejected by the left ventricle and the reflected wave from the lower body. The pulse waveform of the dashed box in Figure 5d is magnified in Figure 5e, indicating the percussion wave (P-wave), tidal wave (T-wave) and dicrotic wave (D-wave). From the first two peaks, P_1 (t_1) and P_2 (t_2), we can derive two of the most common parameters for arterial stiffness diagnosis: The ratio P_1/P_2 is the radial artery augmentation index (AI_r), and ΔT_{DVP} (t_2-t_1) is the time delay between the first two peaks. The calculated AI_r (59%) and ΔT_{DVP} (224 ms) are compatible with the expected levels for a healthy adult male in his early thirties age.[50] Prolonged pulse record to 200 s proved the signal consistency using the S-patch sensor (Figure S21).

To demonstrate the advantage of the self-adhesive S-patch in on-skin biomechanical sensing, we continued the same pulse monitoring, except interferences of skin vibration and under-water condition were introduced, as seen in panels f and g, respectively, of Figure 5. Under these two extreme conditions, the S-patch could deliver distinguishable pulse waveforms with the characteristic peaks. However, for the PDMS-CNT patch under vibration condition, the waveform pattern was distorted with multiple vibration-generated peaks. We suspected, although the medical tape helped to fix the PDMS-CNT patch on skin, the microscopic poor match at the interface would unleash the vibration-induced impacts between the patch and skin surface. When soaked underwater, the pulse signal from the PDMS-CNT patch was weakened with no discernible characteristic peaks for diagnosis. This might be caused by the infiltration of water into the microgaps between patch and skin, which attenuated the mechanical force transfer. The biomechanical signal quality comparison is summarized in Figure 5h: P-wave peak density normalized by P_1 at static

https://doi.org/10.1021/acsnano.2c07097
ACS Nano 2022, 16, 18608−18620

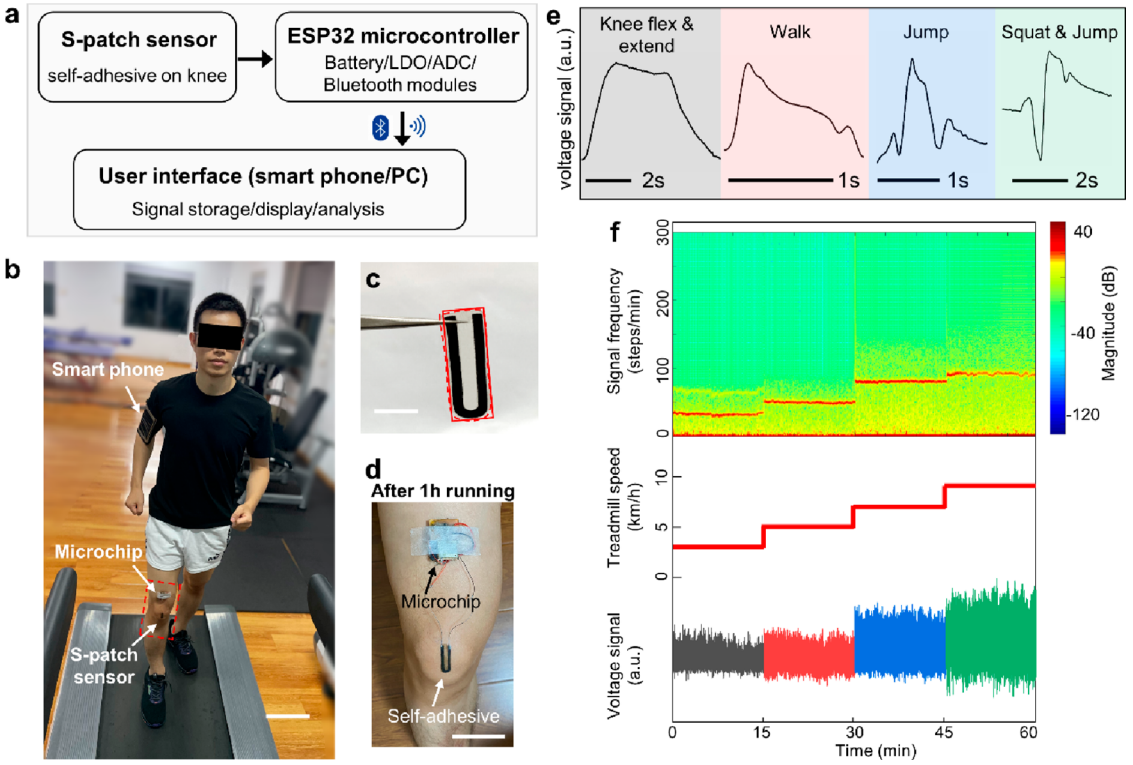

Figure 6. S-patch sensor for knee kinematics monitoring. (a) The workflow diagram of the wireless motion sensing system based on S-patch sensor on knee. (b) Photograph of user wearing smart phone, the self-adhesive S-patch sensor and microchip fixed by medical tape. Scale bar, 15 cm. (c) Photograph of the S-patch sensor on knee. Size is 10 × 26 mm^2. Scale bar, 1 cm. (d) Photograph shows the firm adhesion of S-patch sensor on skin after 1 h of running. Scale bar, 5 cm. (e) Characteristic voltage signal patterns of different knee motions with icons for description. (f) Voltage signal, treadmill speed, and time-frequency domain analysis for a volunteer running continually at increasing treadmill speed of 3, 5, 7, and 9 km/h

condition, and the waveform fidelity. Obviously, under interferences, the P-wave intensity recorded by the S-patch was more consistent than that by the PDMS-CNT patch, and the waveform fidelity for characteristic peaks identification was always available for the S-patch sensor. Such interference immunity of the S-patch sensor probably stems from the seamless interlocking effect, which guarantees the uninterrupted biomechanical signal transmission against disturbances.

Long-Duration, Wireless, and Smart Knee Kinematics Monitoring. Unlike a subtle wrist pulse signal, human knee motions involve frequent, drastic skin stretch deformation and severe sweating, which pose a formidable challenge for on-skin strain sensors to maintain tight adhesion. The S-patch was employed as a self-adhesive on-knee sensor for a wireless and smart knee kinematics sensing system, as shown in Figure 6a (see electric circuit diagram in Figure S22). The electrical signal was collected by a ESP32 microcontroller and transmitted to a smartphone through Bluetooth for motion analysis. A volunteer equipped with this system ran ceaselessly on a treadmill at increasing speed of 3, 5, 7, and 9 km/h for 1 h, as seen in Figure 6b. Figure 6c shows the lightweight and stretchable U-shaped S-patch. After 1 h of running, the S-patch still firmly adhered on the skin as seen in Figure 6d, ensuring the continuous biomechanical signal collection.

On the one hand, for various kinds of knee motions, including knee flexing and extending, walking, jumping, and jumping from squatting position, the S-patch was able to report characteristic patterns of voltage signal as seen in Figure 6e (repeatable signals in Figure S23), enabling easy identification of the specific motion state. On the other hand, for 1 h running at step-by-step increasing speed, the S-patch sensor managed to collect the motion signals continuously, as shown in Figure 6f, and the spectrogram analysis of the recorded pristine voltage signal (detailed pattern in Figure S24 clearly exhibited step-by-step increasing signal frequencies from 32.4 steps/min at 3 km/h to 91.6 steps/min at 9 km/h These results suggest that the S-patch sensor is not only qualified to differentiate multiple motion modes, but also reliable for long-duration monitoring of vigorous exercise.

CONCLUSION

On-skin biopotential and biomechanical signals provide fundamental information for human healthcare assessments. However, reliable epidermal electrodes for capturing high-quality signals, especially under extreme conditions, remains a daunting challenge, which hinders the precise and ambulatory monitoring of physiological status. We reported a facile fabrication scheme for dry epidermal patches based on the incorporation of CNT percolation network into a synthesized supramolecular polymer. The epidermal patches accorded skin-like softness, good elasticity, structural/electrical self-repairment, and robust on-skin adhesion in a signal platform. The combined attributes enable the epidermal patches to secure the high-quality biopotential and biomechanical signals against harsh interferences (e.g., motion artifacts, underwater use). ECG recording under various disturbances, machine-learning-enabled hand gesture recognition through EMG testing, radial artery pulse and knee kinematics sensing, were successfully demonstrated, proving their versatile utility in physiological monitoring. The SESA-based epidermal patches promise to

https://doi.org/10.1021/acsnano.2c07097
ACS Nano 2022, 16, 18608−18620

provide feasible solutions to reliable and robust monitoring of ambulatory and continuous healthcare status.

METHODS

Synthesis of the SESA Polymer. The synthesis was modified from a previously reported method.[51] First, 5 g of ALA powder (Adamas, 13428D) was heated at 140 °C until it turned into a liquid-like melt. Then, 0.4 g of MBAA (Sigma-Aldrich, 146072) was added into the ALA melt and dissolved under magnetic stirring for 5 min. Lastly, 1.2 mg of $FeCl_3$ (Sigma-Aldrich,157740) was added into the melt and stirred for 10 min to get a yellowish and transparent liquid. This liquid mix was then cooled to room temperature to solidify into the SESA polymer.

Fabrication of SESA-Based Epidermal Patches (J-Patch and S-Patch) and PDMS-CNT Electrode. PDMS substrate was modified with poly dopamine to obtain a highly hydrophilic surface for homogeneous deposition of aqueous CNT dispersion, according to a reported method.[52] Aqueous CNT solution was prepared by sonicating 0.2 g of multiwalled CNT (Nanjing XFNANO) and 0.04g Sodium dodecyl sulfate (Sigma-Aldrich, 436143) in 125 mL of distilled water. The aqueous CNT dispersion was sprayed on pd-PDMS, and the sheet resistance of the CNT percolation network was controlled by spray-coating cycles (1 s for each cycle). The pd-PDMS was fixed on a hot plate (120 °C) to dry the CNT film. SESA polymer was melted at 120 °C and poured above the CNT film. Scotch tapes with tunable thickness was used as spacer and another PDMS substrate was pressed on top. After cooling, the SESA-CNT composite film was peeled off to obtain the J-patch. Another SESA layer was coated on the J-patch at the CNT film side, using similar procedures, to get the S-patch. For fabrication of PDMS-CNT electrode, aqueous CNT dispersion was sprayed for 10 cycles on glass slide which was fixed on a hot plate (120 °C) to dry the CNT film. Liquid PDMS prepolymer was coated on the CNT film and cured at 80 °C for 2h. Scotch tape was used as a spacer to control the thickness of PDMS-CNT electrode to be around 140 μm. In electrode-skin impedance test and pulse sensing, PDMS-CNT electrodes were attached on forearm skin using medical tape for fixation.

Spectroscopic Analysis, Morphological Characterization, Thermal Analysis, Rheological, and Mechanical Tests. XRD test was performed using diffractometer (GADDS XRD system, Bruker AXS). A Raman test was conducted with a DXR Raman Microscope (Thermal Scientific Corporation, USA, with a 780 nm excitation length). A FTIR test was completed using an IR Prestige-21 by Shimadzu. SEM characterization was accomplished using a JEOL JSM-7001F field emission scanning electron microscope. AFM measurements were conducted on a commercial scanning probe microscopy (SPM) system (MPF-3D, Asylum Research, Oxford Instrument) with a silicon tip (AC240 PP, Olympus). TGA test was conducted from 30 to 450 °C at a temperature rate of 10 °C min^{-1} using DTG-60H (Shimadzu). The 3D surface profiles of PDMS skin replica and J-patch surface (contact side with fingertip) were measured using an OLS5000 laser confocal microscope. DSC test was performed from −80 to 20 °C at a temperature rate of 10 °C min^{-1} using a differential scanning calorimeter (DSC Q200, TA Instruments). The temperature-related rheological tests were performed using a MCR302 rheometer (Anton Paar). Viscometry measurements were carried out over a shear rate of 1 s^{-1} from 120 to 25 °C. Oscillatory sweeps were performed at 1 Hz within shear strain of 5% from 120 to 25 °C. In mechanical tests, strip-shaped samples ($20 \times 5 \times 1$ mm^3) of SESA gel, J-patch, and S-patch were strained at constant stretching and releasing speed of 20 mm/min using a universal testing machine (MultiTest-i, Mecmesin).

Adhesion Strength Characterization. 90 deg peeling tests were used to evaluate the adhesion strength, using a customized universal testing machine. For adhesive tests on forearm skin, strip-shaped S-patch, J-patch and four types of commercial medical tapes (from suppliers of Watsons, Guardian, and 3M) were attached on volunteer's forearm skin. At a stretching speed of 50 mm/min, the measured peeling forces per width of the tested samples were recorded and the adhesive strength was determined by dividing the plateau force by the width of the samples. To prevent excessive tensile stretching of tested samples during peeling process, 70 μm thick Kapton films were glued to the stretchable samples (S-patch, J-patch and Watsons plastic surgical tape) to works as stiff backing. Before the peeling test, sweat was removed to allow direct contact of patch electrode with human skin. For adhesive strength tests in cyclic, stretching, and underwater conditions, fresh porcine skins were cleaned with ethanol on the surface and dried before attachment with J-patch and S-patch.

Biopotential Sensing. The electrode−skin interfacial impedance was measured with the dual-electrode method using an electrochemical analyzer (CHI660E) over a frequency range from 1 to 10^4 Hz at a voltage of 100 mV. Two electrodes were placed on forearm skin with a separation of 10 cm. J-patches, commercial gel electrodes (Chunfeng YD-50 Ag/AgCl gel electrodes) and PDMS-CNT electrodes were used for comparison. To record ECG signals, two electrodes (J-patches and commercial gel electrodes) were placed on each forearm, and one reference electrode on the belly. ECG signals were measured by a Heal Force PC-80B ECG Monitor. We performed signal analysis (root-mean-square/spectrogram/fast-Fourier transform) on the collected ECG data using signal processing algorithms in Matlab. EMG signals were collected with a sampling frequency of 1000 Hz (ZJE-II, China).

Data Collection and Machine-Learning Models. The EMG voltage signals from the J-patch electrode were acquired during hand gesture formation. Concerning the individual gesture recognition, 1400 samples in voltage channel (V) were collected for each gesture ("High-five", "Claw", "OK", "Good job", "Victory", and "Rock on"). Then, the other two features were indirectly acquired from time-differential voltages (dV/dt and d^2V/dt^2) based upon electrical kinetics of biosignals and formed into one group data (4200 samples for per gesture). After that, a whole data set was built from 6 gestures, with a total number of 25 200 samples. There are 4 groups of data used for analysis: 3 groups for training and 1 group for prediction. The data training models were configured as follows: the principal component analysis (PCA) was used to implement the features for training, the Ensemble classifier (Bagged Trees) was employed for data classification, and the confusion chart was obtained after training. The prediction data analyzed with trained model was used for accuracy calculation and plotting confusion map. The prediction accuracy was generally used to evaluate the model training results. The training models were developed in MATLAB and Python.

Biomechanical Sensing. To investigate the strain sensing properties of the S-patch, a digital multimeter (Keithley DMM6500 6 1/2-Digit Bench/System) was used to record the electrical resistance variation while a high-precision motorized linear stage (LEYG, Electric Actuator, SMC) was used to impose different strain stimuli on the S-patch sensor. To assess the antivibration performance of S-patch and PDMS-CNT patch sensors in subtle biomechanical signal sensing, a coin button-type cellphone vibration micromotor with a 1 cm diameter was used to generate analogous skin shaking. The vibrator works at a direct voltage of 3 V, and the rated speed is about 12 000 ± 2500 rpm. The skin oscillation amplitude is about 1.5 mm. The vibrator was attached on the forearm near the sensor position (2 cm distance) while S-patch or PDMS-CNT patch sensors were employed to capture the radial artery pulse signals. In knee kinematics monitoring, the S-patch was self-adhered to the skin at knee, and the microcontroller microchip was fixed on the skin using medical tapes.

ASSOCIATED CONTENT

Supporting Information

The Supporting Information is available free of charge at https://pubs.acs.org/doi/10.1021/acsnano.2c07097.

Photographs of SESA polymer; XRD characterization; Raman spectra; FTIR spectra; contact angle tests; sheet resistance of spray-coated CNT percolation network;

https://doi.org/10.1021/acsnano.2c07097
ACS Nano 2022, 16, 18608−18620

cross-sectional SEM images; TGA characterization; DSC curve; stress−strain curves of original SESA polymer and self-healed samples; the comparison of self-healing ability; long duration use of J-patch on skin; 3D laser-scanning microscopic image; typical 90 deg peeling test; equivalent circuit diagram of the SESA-CNT electrode and skin interface; EMG signals during hand gesture formation; strain sensing signal reproducibility; durability in strain sensing; 200s sensing signal of radial artery pulse; electric circuit diagram of the wireless and smart knee kinematics monitoring system; voltage signal of on-skin S-patch sensor (PDF)

AUTHOR INFORMATION

Corresponding Author

Ghim Wei Ho − *Department of Electrical and Computer Engineering, National University of Singapore, Singapore 117583, Singapore;* orcid.org/0000-0003-1276-0165; Email: elehgw@nus.edu.sg

Authors

Yin Cheng − *Department of Electrical and Computer Engineering, National University of Singapore, Singapore 117583, Singapore; The State Key Laboratory of High Performance Ceramics and Superfine Microstructure, Shanghai Institute of Ceramics, Chinese Academy of Science, Shanghai 200050, China*

Yi Zhou − *Department of Electrical and Computer Engineering, National University of Singapore, Singapore 117583, Singapore;* orcid.org/0000-0001-5369-5713

Ranran Wang − *The State Key Laboratory of High Performance Ceramics and Superfine Microstructure, Shanghai Institute of Ceramics, Chinese Academy of Science, Shanghai 200050, China*

Kwok Hoe Chan − *Department of Electrical and Computer Engineering, National University of Singapore, Singapore 117583, Singapore*

Yan Liu − *The State Key Laboratory of High Performance Ceramics and Superfine Microstructure, Shanghai Institute of Ceramics, Chinese Academy of Science, Shanghai 200050, China*

Tianpeng Ding − *Department of Electrical and Computer Engineering, National University of Singapore, Singapore 117583, Singapore*

Xiao-Qiao Wang − *Department of Electrical and Computer Engineering, National University of Singapore, Singapore 117583, Singapore*

Tongtao Li − *Department of Electrical and Computer Engineering, National University of Singapore, Singapore 117583, Singapore;* orcid.org/0000-0003-3576-9533

Complete contact information is available at: https://pubs.acs.org/10.1021/acsnano.2c07097

Author Contributions

#Y.C., Y.Z., and R.W. contributed equally to this work. Y.C. and G.W.H. conceived and designed the experiments; Y.C., Y.Z. and R.W. carried out experiments and collected the overall data; Y.C., K.H.C., Y.L., X.-Q.W., T.D., and T.L. contributed to materials fabrication and characterization. T.D. and G.W.H. analyzed all the data and cowrote the paper. All authors discussed the results and commented on the manuscript.

Notes

The authors declare no competing financial interest.

ACKNOWLEDGMENTS

This research was supported by the Advanced Research and Technology Innovation Centre (ARTIC), the National University of Singapore under Grant (project number: R261-518-014-720), A*STAR under its 2019 AME IRG & YIRG Grant Calls, A2083c0059, National Natural Science Foundation of China (52203365) and Shanghai Pujiang Program (21PJ1414800).

REFERENCES

(1) Kim, D.-H.; Lu, N.; Ma, R.; Kim, Y.-S.; Kim, R.-H.; Wang, S.; Wu, J.; Won, S. M.; Tao, H.; Islam, A.; et al. Epidermal Electronics. *Science* **2011**, *333* (6044), 838−843.

(2) Krishnan, S. R.; Su, C.-J.; Xie, Z.; Patel, M.; Madhvapathy, S. R.; Xu, Y.; Freudman, J.; Ng, B.; Heo, S. Y.; Wang, H.; et al. Wireless, Battery-Free Epidermal Electronics for Continuous, Quantitative, Multimodal Thermal Characterization of Skin. *Small* **2018**, *14* (47), 1803192.

(3) Son, D.; Kang, J.; Vardoulis, O.; Kim, Y.; Matsuhisa, N.; Oh, J. Y.; To, J. W. F.; Mun, J.; Katsumata, T.; Liu, Y.; et al. An integrated self-healable electronic skin system fabricated via dynamic reconstruction of a nanostructured conducting network. *Nat. Nanotechnol.* **2018**, *13* (11), 1057−1065.

(4) Zhao, S.; Zhu, R. Electronic Skin with Multifunction Sensors Based on Thermosensation. *Adv. Mater.* **2017**, *29* (15), 1606151.

(5) Cheng, Y.; Wang, R.; Zhai, H.; Sun, J. Stretchable electronic skin based on silver nanowire composite fiber electrodes for sensing pressure, proximity, and multidirectional strain. *Nanoscale* **2017**, *9* (11), 3834−3842.

(6) Yamada, T.; Hayamizu, Y.; Yamamoto, Y.; Yomogida, Y.; Izadi-Najafabadi, A.; Futaba, D. N.; Hata, K. A stretchable carbon nanotube strain sensor for human-motion detection. *Nat. Nanotechnol.* **2011**, *6* (5), 296−301.

(7) Cheng, Y.; Wang, R.; Sun, J.; Gao, L. A Stretchable and Highly Sensitive Graphene-Based Fiber for Sensing Tensile Strain, Bending, and Torsion. *Adv. Mater.* **2015**, *27* (45), 7365−7371.

(8) Lee, E. K.; Kim, M. K.; Lee, C. H. Skin-Mountable Biosensors and Therapeutics: A Review. *Annu. Rev. Biomed. Eng.* **2019**, *21* (1), 299−323.

(9) Liu, Y.; Liu, J.; Chen, S.; Lei, T.; Kim, Y.; Niu, S.; Wang, H.; Wang, X.; Foudeh, A. M.; Tok, J. B.; et al. Soft and elastic hydrogel-based microelectronics for localized low-voltage neuromodulation. *Nat. Biomed. Eng.* **2019**, *3* (1), 58−68.

(10) Zhang, S.; Li, S.; Xia, Z.; Cai, K. A review of electronic skin: soft electronics and sensors for human health. *J. Mater. Chem. B* **2020**, *8* (5), 852−862.

(11) Holzapfel, G. A. Biomechanics of Soft Tissue. In *The Handbook of Materials Behavior Models*, 1st ed; Lemaitre, J., Ed.; Academic Press: Boston, 2001; Vol. 3, pp 1049−1063.

(12) Kalra, A.; Lowe, A.; Al-Jumaily, A. M. Mechanical Behaviour of Skin: A Review. *J. Mater. Sci. Eng.* **2016**, *5*, 1−7.

(13) Wang, Y.; Lee, S.; Yokota, T.; Wang, H.; Jiang, Z.; Wang, J.; Koizumi, M.; Someya, T. A durable nanomesh on-skin strain gauge for natural skin motion monitoring with minimum mechanical constraints. *Science Advances* **2020**, *6* (33), No. eabb7043.

(14) Kang, J.; Son, D.; Wang, G.-J. N.; Liu, Y.; Lopez, J.; Kim, Y.; Oh, J. Y.; Katsumata, T.; Mun, J.; Lee, Y.; et al. Tough and Water-Insensitive Self-Healing Elastomer for Robust Electronic Skin. *Adv. Mater.* **2018**, *30* (13), 1706846.

(15) Su, G.; Yin, S.; Guo, Y.; Zhao, F.; Guo, Q.; Zhang, X.; Zhou, T.; Yu, G. Balancing the mechanical, electronic, and self-healing properties in conductive self-healing hydrogel for wearable sensor applications. *Materials Horizons* **2021**, *8* (6), 1795−1804.

(16) Darabi, M. A.; Khosrozadeh, A.; Mbeleck, R.; Liu, Y.; Chang, Q.; Jiang, J.; Cai, J.; Wang, Q.; Luo, G.; Xing, M. Skin-Inspired

Multifunctional Autonomic-Intrinsic Conductive Self-Healing Hydrogels with Pressure Sensitivity, Stretchability, and 3D Printability. *Adv. Mater.* **2017**, *29* (31), 1700533.
(17) Wang, Y.; Sun, S.; Wu, P. Adaptive Ionogel Paint from Room-Temperature Autonomous Polymerization of α-Thioctic Acid for Stretchable and Healable Electronics. *Adv. Funct. Mater.* **2021**, *31* (24), 2101494.
(18) Cheng, Y.; Chan, K. H.; Wang, X.-Q.; Ding, T.; Li, T.; Zhang, C.; Lu, W.; Zhou, Y.; Ho, G. W. A Fast Autonomous Healing Magnetic Elastomer for Instantly Recoverable, Modularly Programmable, and Thermorecyclable Soft Robots. *Adv. Funct. Mater.* **2021**, *31* (32), 2101825.
(19) Li, X.; He, L.; Li, Y.; Chao, M.; Li, M.; Wan, P.; Zhang, L. Healable, Degradable, and Conductive MXene Nanocomposite Hydrogel for Multifunctional Epidermal Sensors. *ACS Nano* **2021**, *15* (4), 7765−7773.
(20) Zhou, X.; Rajeev, A.; Subramanian, A.; Li, Y.; Rossetti, N.; Natale, G.; Lodygensky, G. A.; Cicoira, F. Self-healing, stretchable, and highly adhesive hydrogels for epidermal patch electrodes. *Acta Biomater* **2022**, *139*, 296−306.
(21) Guo, H.; Han, Y.; Zhao, W.; Yang, J.; Zhang, L. Universally autonomous self-healing elastomer with high stretchability. *Nat. Commun.* **2020**, *11* (1), 2037.
(22) Wu, J.; Cai, L.-H.; Weitz, D. A. Tough Self-Healing Elastomers by Molecular Enforced Integration of Covalent and Reversible Networks. *Adv. Mater.* **2017**, *29* (38), 1702616.
(23) Zhang, L.; Kumar, K. S.; He, H.; Cai, C. J.; He, X.; Gao, H.; Yue, S.; Li, C.; Seet, R. C.-S.; Ren, H.; Ouyang, J.; et al. Fully organic compliant dry electrodes self-adhesive to skin for long-term motion-robust epidermal biopotential monitoring. *Nat. Commun.* **2020**, *11* (1), 4683.
(24) Meng, L.; Fu, Q.; Hao, S.; Xu, F.; Yang, J. Self-adhesive, biodegradable silk-based dry electrodes for epidermal electrophysiological monitoring. *Chem. Eng. J.* **2022**, *427*, 131999.
(25) Tang, W.; Zhou, Y.; Chen, S.; Yu, S.; Yang, Y.; Lin, J.; Yin, S.; Ma, Y.; Hu, B. Delamination-Resistant Imperceptible Bioelectrode for Robust Electrophysiological Signals Monitoring. *ACS Materials Letters* **2021**, *3* (9), 1385−1393.
(26) Kim, D. H.; Viventi, J.; Amsden, J. J.; Xiao, J.; Vigeland, L.; Kim, Y. S.; Blanco, J. A.; Panilaitis, B.; Frechette, E. S.; Contreras, D.; et al. Dissolvable films of silk fibroin for ultrathin conformal bio-integrated electronics. *Nat. Mater.* **2010**, *9* (6), 511−517.
(27) Nur, R.; Matsuhisa, N.; Jiang, Z.; Nayeem, M. O. G.; Yokota, T.; Someya, T. A Highly Sensitive Capacitive-type Strain Sensor Using Wrinkled Ultrathin Gold Films. *Nano Lett.* **2018**, *18* (9), 5610−5617.
(28) Ho, M. D.; Ling, Y.; Yap, L. W.; Wang, Y.; Dong, D.; Zhao, Y.; Cheng, W. Percolating Network of Ultrathin Gold Nanowires and Silver Nanowires toward "Invisible" Wearable Sensors for Detecting Emotional Expression and Apexcardiogram. *Adv. Funct. Mater.* **2017**, *27* (25), 1700845.
(29) Nawrocki, R. A.; Jin, H.; Lee, S.; Yokota, T.; Sekino, M.; Someya, T. Self-Adhesive and Ultra-Conformable, Sub-300 nm Dry Thin-Film Electrodes for Surface Monitoring of Biopotentials. *Adv. Funct. Mater.* **2018**, *28* (36), 1803279.
(30) Kabiri Ameri, S.; Ho, R.; Jang, H.; Tao, L.; Wang, Y.; Wang, L.; Schnyer, D. M.; Akinwande, D.; Lu, N. Graphene Electronic Tattoo Sensors. *ACS Nano* **2017**, *11* (8), 7634−7641.
(31) Zhao, Y.; Zhang, S.; Yu, T.; Zhang, Y.; Ye, G.; Cui, H.; He, C.; Jiang, W.; Zhai, Y.; Lu, C.; Gu, X.; Liu, N. Ultra-conformal skin electrodes with synergistically enhanced conductivity for long-time and low-motion artifact epidermal electrophysiology. *Nat. Commun.* **2021**, *12* (1), 4880.
(32) Wu, H.; Yang, G.; Zhu, K.; Liu, S.; Guo, W.; Jiang, Z.; Li, Z. On-Skin Electrodes: Materials, Devices, and Systems of On-Skin Electrodes for Electrophysiological Monitoring and Human−Machine Interfaces. *Advanced Science* **2021**, *8* (2), 2170007.
(33) Deng, J.; Yuk, H.; Wu, J.; Varela, C. E.; Chen, X.; Roche, E. T.; Guo, C. F.; Zhao, X. Electrical bioadhesive interface for bioelectronics. *Nat. Mater.* **2021**, *20* (2), 229−236.
(34) Myers, A. C.; Huang, H.; Zhu, Y. Wearable silver nanowire dry electrodes for electrophysiological sensing. *RSC Adv.* **2015**, *5* (15), 11627−11632.
(35) Wang, K.; Parekh, U.; Pailla, T.; Garudadri, H.; Gilja, V.; Ng, T. N. Stretchable Dry Electrodes with Concentric Ring Geometry for Enhancing Spatial Resolution in Electrophysiology. *Adv. Healthc. Mater.* **2017**, *6* (19), 1700552.
(36) Liu, L.; Li, H. Y.; Fan, Y. J.; Chen, Y. H.; Kuang, S. Y.; Li, Z. B.; Wang, Z. L.; Zhu, G. Nanofiber-Reinforced Silver Nanowires Network as a Robust, Ultrathin, and Conformable Epidermal Electrode for Ambulatory Monitoring of Physiological Signals. *Small* **2019**, *15* (22), No. 1900755.
(37) Xu, Y.; Sun, B.; Ling, Y.; Fei, Q.; Chen, Z.; Li, X.; Guo, P.; Jeon, N.; Goswami, S.; Liao, Y.; et al. Multiscale porous elastomer substrates for multifunctional on-skin electronics with passive-cooling capabilities. *Proc. Natl. Acad. Sci. U S A* **2020**, *117* (1), 205−213.
(38) Romero, F. J.; Castillo, E.; Rivadeneyra, A.; Toral-Lopez, A.; Becherer, M.; Ruiz, F. G.; Rodriguez, N.; Morales, D. P. Inexpensive and flexible nanographene-based electrodes for ubiquitous electrocardiogram monitoring. *npj Flexible Electronics* **2019**, 3 (1), 12.
(39) Kim, J. H.; Kim, S. R.; Kil, H. J.; Kim, Y. C.; Park, J. W. Highly Conformable, Transparent Electrodes for Epidermal Electronics. *Nano Lett.* **2018**, *18* (7), 4531−4540.
(40) Pan, S.; Zhang, F.; Cai, P.; Wang, M.; He, K.; Luo, Y.; Li, Z.; Chen, G.; Ji, S.; Liu, Z.; Loh, X. J.; Chen, X. Mechanically Interlocked Hydrogel−Elastomer Hybrids for On-Skin Electronics. *Adv. Funct Mater.* **2020**, *30* (29), 1909540.
(41) Zhang, W.; Wu, B.; Sun, S.; Wu, P. Skin-like mechanoresponsive self-healing ionic elastomer from supramolecular zwitterionic network. *Nat. Commun.* **2021**, *12* (1), 4082.
(42) Xu, J.; Chen, P.; Wu, J.; Hu, P.; Fu, Y.; Jiang, W.; Fu, J. Notch-Insensitive, Ultrastretchable, Efficient Self-Healing Supramolecular Polymers Constructed from Multiphase Active Hydrogen Bonds for Electronic Applications. *Chem. Mater.* **2019**, *31* (19), 7951−7961.
(43) Luo, J.; Xing, Y.; Sun, C.; Fan, L.; Shi, H.; Zhang, Q.; Li, Y.; Hou, C.; Wang, H. A bio-adhesive ion-conducting organohydrogel as a high-performance non-invasive interface for bioelectronics. *Chem. Eng. J.* **2022**, *427*, 130886.
(44) Wang, S.; Cheng, H.; Yao, B.; He, H.; Zhang, L.; Yue, S.; Wang, Z.; Ouyang, J. Self-Adhesive, Stretchable, Biocompatible, and Conductive Nonvolatile Eutectogels as Wearable Conformal Strain and Pressure Sensors and Biopotential Electrodes for Precise Health Monitoring. *Acs. Appl. Mater. Inter.* **2021**, *13* (17), 20735−20745.
(45) Ranamukhaarachchi, S. A.; Lehnert, S.; Ranamukhaarachchi, S. L.; Sprenger, L.; Schneider, T.; Mansoor, I.; Rai, K.; Häfeli, U. O.; Stoeber, B. A micromechanical comparison of human and porcine skin before and after preservation by freezing for medical device development. *Sci. Rep.* **2016**, *6* (1), 32074.
(46) Zhang, Q.; Fu, L.; Gu, L. A Cascaded Convolutional Neural Network for Assessing Signal Quality of Dynamic ECG. *Comput. Math. Method. M.* **2019**, *2019*, 7095137.
(47) Uchaipichat, N.; Thanawattano, C.; Buakhamsri, A. The Development of ST-Episode Detection in Holter Monitoring for Myocardial Ischemia. *Procedia Computer Science* **2016**, *86*, 188−191.
(48) Amjadi, M.; Yoon, Y. J.; Park, I. Ultra-stretchable and skin-mountable strain sensors using carbon nanotubes−Ecoflex nanocomposites. *Nanotechnology* **2015**, *26* (37), 375501.
(49) Kanoun, O.; Bouhamed, A.; Ramalingame, R.; Bautista-Quijano, J. R.; Rajendran, D.; Al-Hamry, A. Review on Conductive Polymer/CNTs Nanocomposites Based Flexible and Stretchable Strain and Pressure Sensors. *Sensors* **2021**, *21* (2), 341.
(50) Nichols, W. W. Clinical measurement of arterial stiffness obtained from noninvasive pressure waveforms. *Am. J. Hypertens* **2005**, *18* (S1), 3S−10S.
(51) Zhang, Q.; Shi, C.-Y.; Qu, D.-H.; Long, Y.-T.; Feringa, B. L.; Tian, H. Exploring a naturally tailored small molecule for stretchable,

https://doi.org/10.1021/acsnano.2c07097
ACS Nano 2022, 16, 18608−18620

self-healing, and adhesive supramolecular polymers. *Science Advances* **2018**, *4* (7), No. eaat8192.
(52) Akter, T.; Kim, W. S. Reversibly Stretchable Transparent Conductive Coatings of Spray-Deposited Silver Nanowires. *Acs. Appl. Mater. Inter.* **2012**, *4* (4), 1855−1859.

https://doi.org/10.1021/acsnano.2c07097
ACS Nano 2022, 16, 18608−18620